Biological matrix composites from cultured plant cells

Eleftheria Roumeli[a,b] (ORCID), Rodinde Hendrickx[a], Luca Bonanomi[a], Aniruddh Vashisth[c] (ORCID), Katherine Rinaldi[d], and Chiara Daraio[a,1] (ORCID)

We present an approach to fabricate biological matrix composites made entirely from cultured plant cells. We utilize the cell's innate ability to synthesize nanofibrillar cell walls, which serve as the composite's fundamental building blocks. Following a controlled compression/dehydration process, the cells arrange into lamellar structures with hierarchical features. We demonstrate that the native cell wall nanofibrils tether adjacent cells together through fibrillar interlocking and intermolecular hydrogen bonding. These interactions facilitate intercellular adhesion and eliminate the need for other binders. Our fabrication process utilizes the entire plant cell, grown in an in vitro culture; requires no harsh chemical treatments or waste-generating extraction or selection processes; and leads to bulk biocomposites that can be produced in situ and biodegrade in soil. The final mechanical properties are comparable to commodity plastics and can be further modulated by introducing filler particles.

sustainable materials | biocomposites | biopolymers

Biocomposites have the potential to meet global material demand with renewable resources and with reduced life cycle environmental impacts, compared with common petroleum-based materials (1, 2). However, today's green composites, which primarily derive from crops and plant fibers, still rely on matrices or binders derived from petroleum or on harsh thermal, mechanical, and chemical treatment of mature plants (3, 4). Most recently, self-growing biocomposites have been proposed as a new class of multifunctional materials, which capitalize on the ability of living matter to self-fabricate and replicate (5–7). Bacteria often serve as a fabrication platform for pure nanocellulose (6, 8) and polyesters (9). Some of the strongest and stiffest cellulose materials are made from bacteria cultures (10, 11). More complex eukaryotic organisms, such as fungi and fermenting yeast, have also been used in biocomposites. These approaches minimize waste as no part of the cell is discarded, reduce production and harvest time, and avoid environmentally harmful postprocessing steps (12–14). Remarkably, mycelium materials have already reached the market for protective packaging, insulation, and acoustic panels (12, 15–17). However, the main drawback of existing nonchemically processed eukaryotic biocomposites is that they have low mechanical performance [modulus < 1 GPa and strength < 10 MPa (12, 18)], which renders them unsuitable for engineering and structural applications. Plant materials demonstrate an impressive range of mechanical properties. Their stiffness and strength, for example, can vary over three orders of magnitude (19). This remarkable range depends on the plant's composition and hierarchical organization with nanoscale arrangement of biopolymers within the cell wall and the distinct microscale patterning at the cell level (*SI Appendix*) (19). Wood products, like medium-density fiberboard (MDF), combine wood shavings with additives or binders, to expand their potential uses. Recently, chemical and/or thermomechanical postprocessing of natural wood has been adopted to create high-performance materials, with properties comparable to steel, ceramics, and insulating foams (20–24). However, these materials' require chemical treatment such as processing in $NaOH/Na_2SO_3$ or H_2O_2 solutions for removal of most noncellulose components of wood (24), which are energy-intensive treatments and produce waste.

Here we describe an approach to fabricate biocomposite materials based on the gradual dehydration and compression of cultured plant cells. Our approach produces no waste and reduces processing energy requirements, using only low-pressure filtration and oven drying at mild temperatures (60° C). We use undifferentiated tobacco cells as a model system. These cells multiply rapidly (a factor of approximately 80 to 100 every 7 d) (25), can be used to produce materials in situ, are independent of seasonality and local climate at production site, require no extraction processes, and can be cold pressed in molds of different shapes and sizes. Our materials retain the native plant cell wall composition and nanofibrillar structure naturally secreted by growing plant cells and obtain a lamellar microstructure induced by the compression process. The obtained densified bulk biocomposites achieve Young's modulus and strength comparable to structural and engineered woods and commodity plastics. We characterize the microstructure, composition, and mechanical properties of the produced materials and demonstrate that

Significance

The development of novel degradable biocomposites can contribute to answering the increasing global demand for sustainable materials. We present a method to obtain self-bonded biocomposite materials from cultured plant cells. Subjecting cells to a cold-compression molding process creates hierarchical biocomposites that have stiffness and strength comparable to commodity plastics, while being 100% biodegradable in soil. Introducing fillers expands the attainable functionalities, demonstrating the versatility of the proposed platform. The use of fast-growing plant cells offers the benefits of short harvest time, zero biomass waste during processing, in situ manufacturing, and no arable land requirement. The approach allows the possibility of further tuning the final material properties by genetically engineering the processed cells.

[1]To whom correspondence may be addressed. Email: daraio@caltech.edu.

the incorporation of filler additives allows tuning of the material's performance and expands their functionalities, for example, creating magnetic and electrically conductive biocomposite materials.

Results and Discussion

We harvest plant cells from a suspension culture and compress them in a permeable mold, to achieve a densified dehydrated structure (Fig. 1*A* and *Materials and Methods*). During compression, water diffuses through the plant cell wall, and the cell volume is gradually reduced. When the cells reach a dry state, corresponding to an approximate 98% weight loss, the resulting bulk materials (Fig. 1*B*) consist of a hierarchical lamellar stack of compacted cell walls. Cross-section scanning electron microscopy (SEM) images of the resulting material (Fig. 1 *C* and *D*) illustrate the obtained anisotropic microstructure.

We characterize the cell morphology with light and laser scanning confocal microscopy (Fig. 2 *B–D*), which shows that the plant cells are elongated, with a mean length of 170 ± 60 µm and a mean width of 45 ± 10 µm, and are surrounded by a thin primary cell wall. By staining the cells we confirm that the cell walls contain cellulose, pectin, and phenolic compounds (Fig. 2 *B–D*) as expected from this cell type (26, 27) (*Materials and Methods*). Compositional analysis of the dry biocomposite material confirms that it is composed of 15% cellulose, 20% hemicelluloses, 6.8% pectins, and 6.3% phenolic compounds. Literature suggests that in tobacco plant cells the remaining components are lipids, nucleic acids, proteins, and inorganics (ash content), which together account for about 45% of the dry mass (28). Residual water within our samples is gravimetrically determined to be 7 ± 3 wt %. Thus, the process results in a biocomposite material, composed of a heterogeneous mixture of the natural cell wall biopolymers.

SEM and transmission electron microscopy (TEM) observations of the biocomposite materials reveal their hierarchical, anisotropic, and lamellar microstructure composed of compacted plant cells (Fig. 2 *E–H*). TEM demonstrates that the nanofibrillar structure of the primary cell walls is preserved during cell compression and dehydration (Fig. 2 *F* and *G*). Accepted models suggest that the primary cell wall is a multilayered structure consisting of cellulose nanofibrils, arranged in various orientations within each plane (from entirely isotropic to helically aligned, depending on cell type and developmental stage), bound in a matrix of hemicelluloses, pectins, and proteins (29). Even in the case of randomly distributed cellulose nanofibrils in the plane of the wall, the structure is considered highly anisotropic across thickness (30). TEM images of our biocomposites show an average dehydrated cell wall thickness of 185 ± 57 nm and cellulose crystalline nanofibril bundles with diameters 1 to 30 nm being conformed across the consecutive parallel planes (Fig. 2 *G* and *H*). We observe a hierarchical structure: at the supracellular level (micrometer scale), a lamellar microstructure consisting of compacted cells (Fig. 2*E*), and at the subcellular level (nanoscale), an anisotropic, multilayered structure, derived from the natural organization of the cell wall components (Fig. 2 *G* and *H*). High-resolution TEM (HRTEM) images show that the outer nanofibrils of the cell walls tether to the adjacent walls (Fig. 2*H*, dangling fibrils pointed by arrows).

Fourier-transform infrared (FTIR) spectroscopy of hydrated and oven-dried cells and of the compacted biocomposite (Fig. 2*I*) reveals the predominant vibrations of carbohydrates (cellulose, hemicelluloses, and pectin), proteins, and phenolic compounds (26, 27, 31) in all samples (see *SI Appendix*, Table S1, for detailed bond assignment). Comparing the spectra reveals that after processing, the biocomposite maintains all the native cell carbohydrate components and retains the same degree of pectin esterification [indicated by the ratio of the 1,735/1,414 peak intensities (26)] but has a slightly lower amount of protein compared to the living cells [lower intensity of the 1,650 cm^{-1} peak (26)]. Moreover, the red-shifted hydrogen bonding band at 3,000 to 3,700 cm^{-1}, in the dried biocomposite, compared to the hydrated cells, reflects the strong intermolecular hydrogen bonding between the cell wall biopolymers (*SI Appendix*) (32, 33).

Based on HRTEM (Fig. 2*H*) and FTIR (Fig. 2*I*) analyses, we postulate that the cell wall adhesion in our biocomposites is provided by two mechanisms: 1) fibrillar interlocking and 2) intermolecular interactions of the polymer chains in the adjacent parts of the cell walls. Further, considering the role of pectins in the structural adhesion of cells in plants (34), we hypothesize
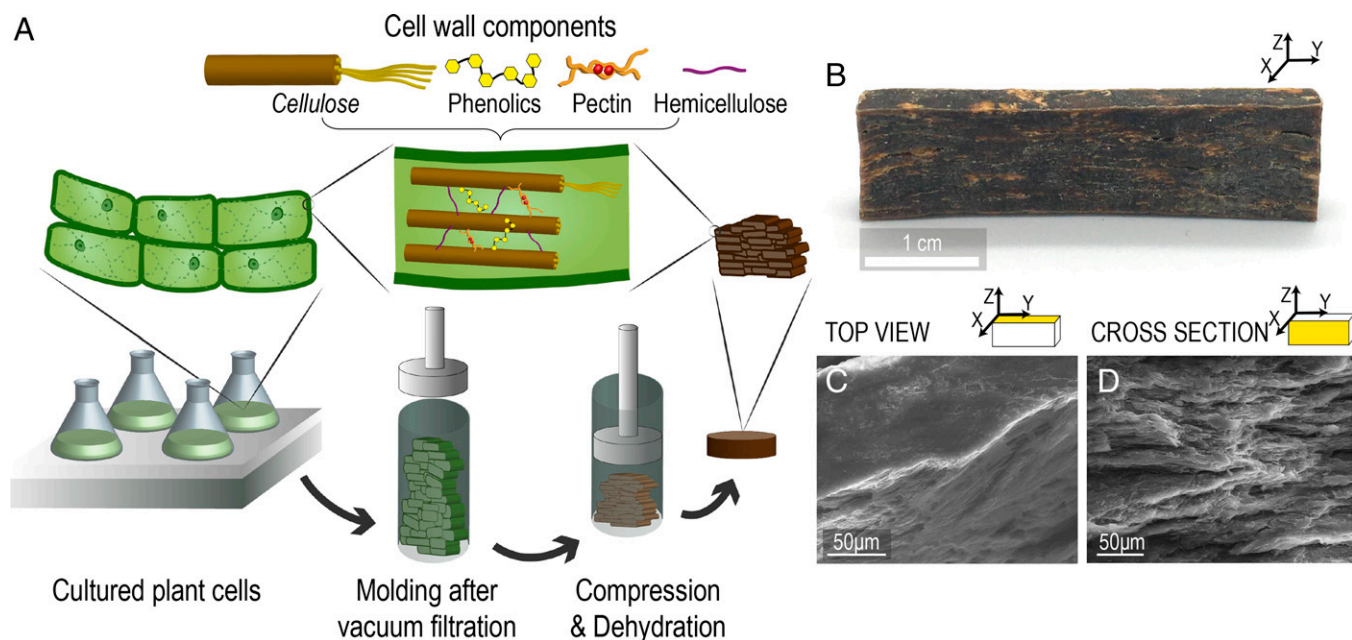

Fig. 1. (*A*) Schematic of the fabrication method. Plant cells are cultured, harvested, and subjected to a controlled compression and dehydration, resulting in a lamellar densified architecture when dried. (*B*) Photograph of the biocomposite. (*C* and *D*) SEM top and cross-sectional views of the anisotropic microstructure.
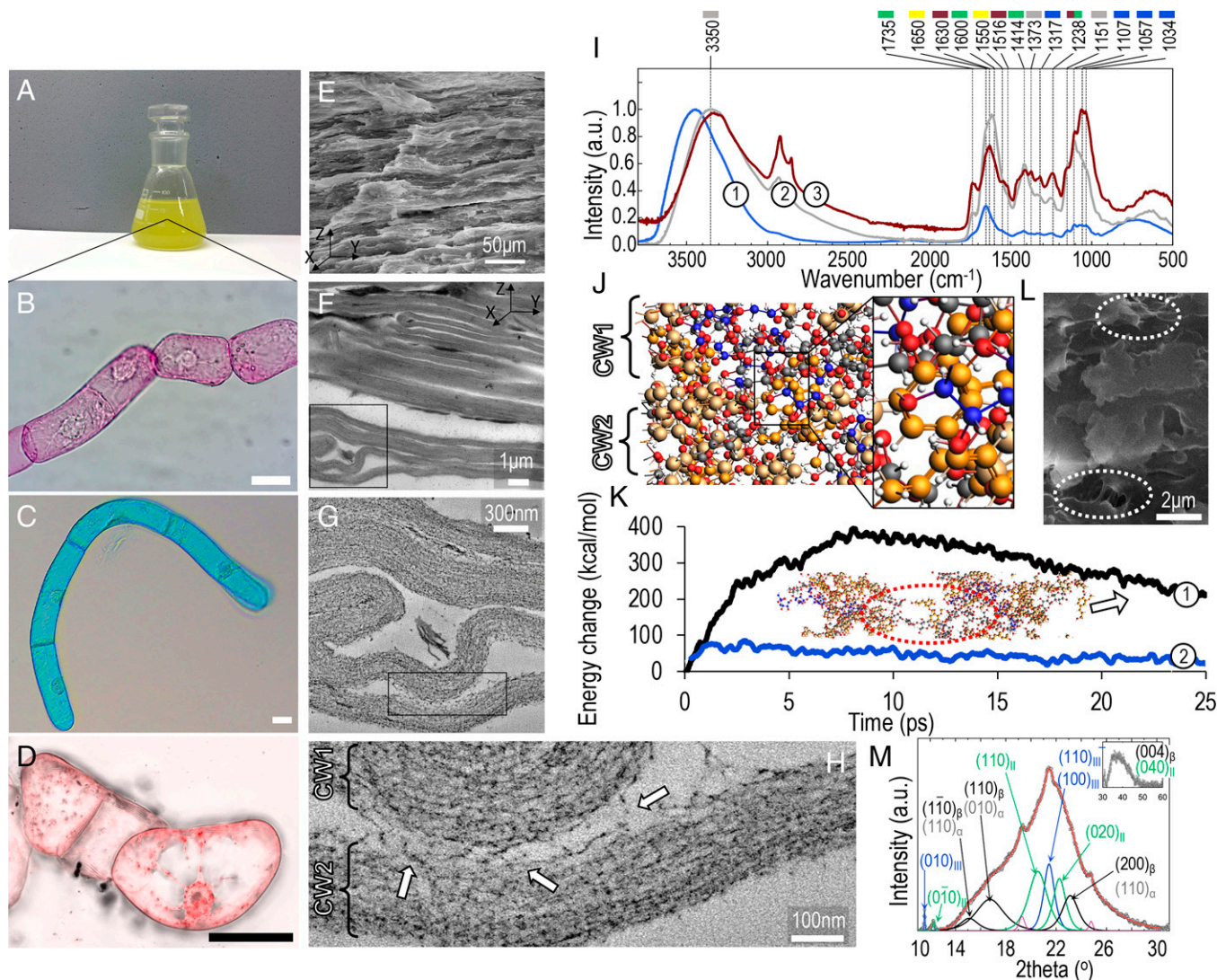
Fig. 2. (*A*) Photograph of the cell culture. Microscopy images of the cells stained for (*B*) pectins, (*C*) cellulose, and (*D*) phenolics. (Scale bars in *B–D*, 20 μm.) (*E*) SEM image of a cross-section, demonstrating the lamellar microstructure. (*F*) TEM and (*G* and *H*) HRTEM images of cross-sections (arrows pointing to dangling fibrils tethering adjacent cell walls, marked as CW1 and CW2). (*I*) FTIR spectra of 1) hydrated cells, 2) dried cells, and 3) dry biocomposite. Color coding for biopolymer peak assignment: gray, all carbohydrates; blue, cellulose; green, pectin; brown, phenolics; and yellow, proteins. (*J*) MD simulation of a fraction of two neighboring cell walls (*Inset* shows pectin and cellulose chains diffused in the adjacent cell wall space). Carbon atoms are colored gray in cellulose, orange in phenolics, yellow in hemicellulose, and blue in pectin chains for clarity. Oxygen atoms are colored red, and hydrogen atoms are white. (*K*) MD results from tensile loading of the compacted cell walls system: 1) total energy and 2) hydrogen bonding energy. *Inset* shows chains being unentangled and pulled out from the space between the two cell walls when subjected to tensile forces. (*L*) SEM of a fractured surface of a tensile-tested biocomposite. (*M*) XRD pattern of the biocomposite with marked contributions from cellulose polymorphs I_α, I_β, II, and III.

that esterified pectins may facilitate this intercellular bonding. We conduct reactive molecular dynamic (MD) simulations (ReaxFF) to verify our hypothesis and study the molecular interactions between adjacent cell walls. Following the fabrication process, we simulate the compression of the outer parts of two neighboring cell walls (Fig. 2 *J* and *K* and *SI Appendix,* Figs. S1–S3). Cell walls are modeled as mixtures of cellulose, hemicellulose, pectin, and phenolics at the ratios identified from chemical analysis. The modeled cell wall polymers encompass all functional groups (-OH, -CO$_2$CH$_3$, -CH$_2$OH, and -COOH) available for intermolecular interactions within the cell walls. The compacted and equilibrated system has a volume of $3.6 \times 2.7 \times 2.5$ nm^3 and shows that all polymer chains at the outer layers of neighboring cell walls interact and diffuse in each other's structure upon compressing. Thus, the compression process leads to molecular interlocking between adjacent cell walls. Then, we subject the system of compacted cell walls to tensile testing, which shows that the total energy has a substantial hydrogen bonding energy component, in agreement

with literature on self-adhesive cellulose materials (35) (Fig. 2*K* and *SI Appendix*, Fig. S3). The fibrillar interlocking leads to chain unfolding (unentanglement) and cascading hydrogen bond breaking and reformation events upon tensile loading (Fig. 2 *K, Inset*) (35, 36). These results match SEM observations of the tensile tested fracture surfaces (Fig. 2*L*), which show fibrils bridging neighboring parts of the matrix.

X-ray diffraction (XRD) patterns of the biocomposite reveal multiple polymorphs of semicrystalline cellulose (I, II, and III, marked in Fig. 2*G*) (23). Native cellulose from plant species crystallizes in the type I polymorphs (I_α, I_β). Regeneration and mercerization, ball-milling in presence of water and other methods (36) lead to the more thermodynamically stable cellulose polymorph II, while ammonia treatment followed by thermal and pressure treatments is known to convert either cellulose I or II to III (37–39). In the densified biocomposites, cellulose microfibrils partially undergo phase transformations to form crystal structures II and III, likely in response to the pressure applied during

dehydration and the changing chemical environment during cell dissociation. We postulate that upon compaction and cell death, protein and nucleic acid losses, as suggested by FTIR, lead to the diffusion of amine-rich compounds from the protoplasm to the extracellular space through the cell walls, thus facilitating the phase transformations, together with the extended period of compression.

We perform tensile and three-point bending tests to characterize the mechanical performance of the dehydrated biocomposites. Since our process results in bulk biopolymer structures, which can serve as a standalone structural material as well as a polymer matrix to be reinforced with fillers, we compare their mechanical properties to 1) bulk synthetic polymers of similar density, which also serve as both a host matrix and unfilled bulk material, and 2) natural and engineered wood, which share similar composition, have a hierarchical structure, and are also used as structural bulk materials. We choose different softwoods (pine), hardwoods (poplar, oak, and walnut), commercial plywood and MDF, and synthetic plastics of similar density (polystyrene [PS], polypropylene [PP], and low-density polyethylene [LDPE]) (Fig. 3 *A*–*C* and *SI Appendix*, Fig. S4). Stress–strain plots obtained from the biocomposites (*SI Appendix*, Fig. S5) show an initial linear elastic response upon loading, both under tension and bending, followed by a brittle failure at small strains (1 $\pm$ 0.3%). The Young's modulus, calculated from the initial linear elastic part of the tension experiments, is 2.5 $\pm$ 0.4 GPa, and the ultimate strength is 21.2 $\pm$ 3 MPa. The flexural modulus is 4.2 $\pm$ 0.4 GPa, and the modulus of rupture is 49.3 $\pm$ 3.2 MPa. Testing the flexural properties of the biocomposite on the two perpendicular planes (see schematic in *SI Appendix*, Fig. S6) reveals that stiffness varies by a factor of ca. 1.75 in the two directions, while strength remains unaffected by orientation. The measured difference in stiffness is due to the anisotropic microstructure of the biocomposite, as discussed above. Tension tests show that our biocomposites are stiffer than the other tested materials (Fig. 3*A*). However, natural woods have higher strength (Fig. 3*B*), which can be explained by their different cellular architectures, cell wall compositions, and component arrangements within the secondary cell walls. The cells

used in our biocomposites originate from the herbaceous plant *Nicotiana tabacum*, and they naturally develop a thin, unlignified primary cell wall (we confirm a low phenolics amount of 6.2 wt %). These cells do not form secondary cell walls and cannot self-organize in a hierarchical microstructure in our in vitro cultures. Regardless, the macroscopic mechanical performance of the biocomposites is comparable to that of commercial engineered woods and commodity plastics. They surpass literature-reported values for bulk, three-dimensional composite biomaterials manufactured through bottom-up methods by eukaryotic organisms that include plant cells, mycelium, or yeast matrixes. All these biocomposites have not been treated to remove native components, and the microorganism cells serve in fact as the building blocks of those materials (12, 13, 18, 20, 40, 43, 44) (Fig. 3*D*). We note, however, that in particular, mycelium-based composites have lower density than our biocomposites (18). Recently, microbial cultured cells (from *Escherichia coli*) were used to create cell-based rigid films through a simple casting and ambient drying method (45). The localized mechanical properties of the microbial films were measured through nanoindentation, revealing a reduced modulus of 5 to 42 GPa and strength values of 60 to 800 MPa (calculated from the measured hardness values). While those properties cannot be directly compared to the plant cell bulk properties we report in our work as they address different length scales, they demonstrate another promising direction for cell-based materials.

A key factor in the design of sustainable materials is their end-of-life fate. The realization of biological matrix materials, such as those described here, offers an environmentally friendly alternative to nondegradable materials, which typically survive in landfills. To assess the biodegradability of our plant-based biocomposites, we perform agricultural soil incubation tests (*Materials and Methods*), comparing their mass loss with that of natural wood (46). Results show an initial mass gain corresponding to water uptake from the soil, in both natural wood and biocomposites (Fig. 3*E*). The detectable mass loss due to biodegradation of the biocomposites begins 3 wk after incubation, while for natural wood it begins about 7 wk later. This can be associated to the presence of lignin in natural wood, which is known to provide resistance to
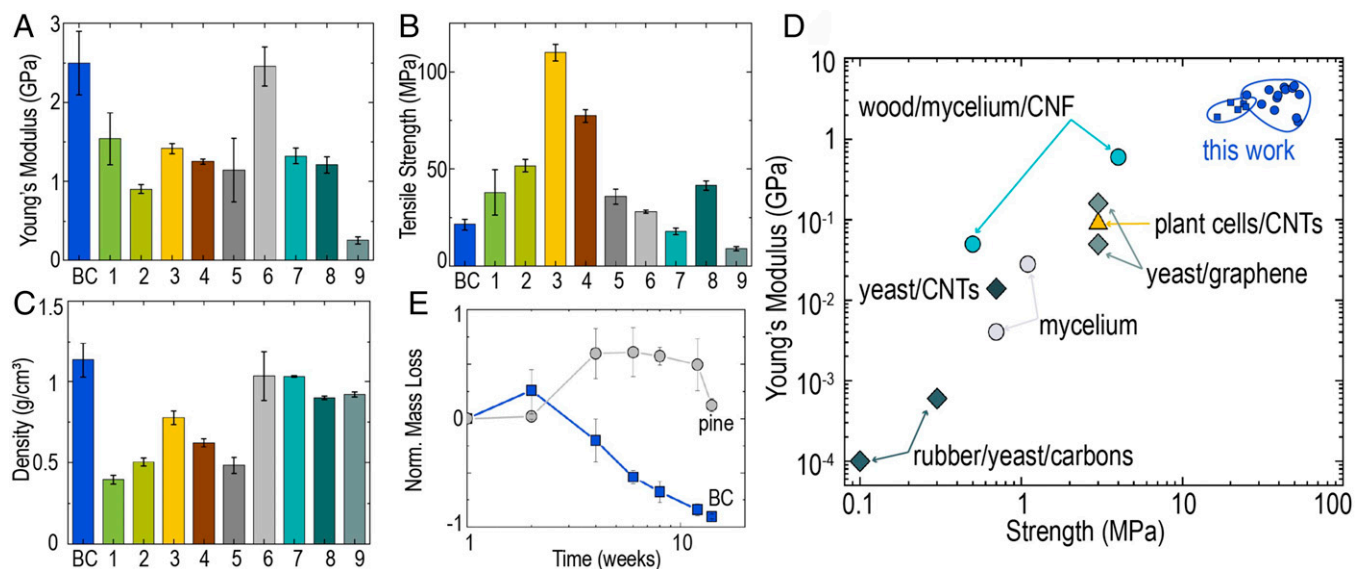

Fig. 3. (*A*) Young's modulus and (*B*) tensile strength of the biocomposite and reference materials. (*C*) Material density. (*D*) Comparison of mechanical properties of this work (blue circles are results from bending tests, and blue squares are results from tensile tests) and literature-reported biocomposites in which microorganism cells serve as a matrix, and their composition and nanostructure have not been altered: yeast-based composites represented with rhombuses and mycelium-based materials with circles (12, 13, 18, 40, 41, 42). (*E*) Biodegradation of the biocomposite and natural pine. Sample notation: BC, pure (without fillers) biocomposite; 1, pine; 2, poplar; 3, oak; 4, walnut; 5, plywood; 6, MDF; 7, PS; 8, PP; 9, LDPE. (Error bars indicate SE for *n* > 5 measurements.) I_α, I_β, II, and III. CNF, cellulose nanofibrils; CNT, carbon nanotubes.

pathogen attacks on cell walls (47) and the water sensitivity of our material. We observe an almost complete biodegradation of the biocomposite 14 wk after initial incubation. A drawback of rapid biodegradation is water sensitivity. We perform water uptake and thickness swelling tests (*SI Appendix*) and find that our biocomposites respond similarly to mycelium/wood biocomposites (18). After more than 24 h of incubation our materials completely disperse in water. However, when stored in ambient conditions, they do not exhibit any swelling or fouling. In applications, the water uptake could be mitigated with surface treatments or water-resistant coatings.

The use of cell cultures for materials fabrication allows on-demand property tuning by interfacing with additive particles (48, 49). We demonstrate the ability to tune and introduce properties in the composites, by incorporating filler additives. The addition of different amounts of natural nanoclay (NC) platelets, for example, changes the biocomposites' compressive modulus and strength (Fig. 4A). Upon the introduction of 0.15 wt % NC the Young's modulus and strength increase by 36 and 87%, respectively. At 0.5 wt % NC the improvements are less significant, 10 and 5%, respectively. At higher NC concentrations both properties are reduced below the values of the unfilled material, which is often observed in polymer nanocomposites because of fillers' aggregation acting as a stress concentrator (52). Different filler particles expand further the biocomposites' property space (Fig. 4B). We plot the Young's modulus as a function of density of different plant cell-based biocomposites: pure cell matrix (BC), biocomposites containing various amounts of carbon fibers (CF), halloysite and montmorillonite NC, and graphene (G). Their properties lie at the intersection of natural cellular materials, including wood-based materials, and commercial plastics (Fig. 4B), presenting Young's moduli spanning over one order of magnitude. We note that our biocomposites are outperformed by pure cellulose materials and densified wood products. This is because our approach preserves the entire natural cell wall composition through mild processing. Filler additives also endow functionalities, such as electrical conductivity or magnetic properties. The electrical conductivity of plant cell/CF composites, for example, can be tuned varying the CF content (Fig. 4C). Similarly, the addition of 13.5 wt % iron oxide nanoparticles (IN) in the plant cell matrix conveys ferromagnetic properties, which allow the biocomposite to support more than five times its weight when attracted by a magnet (Fig. 4D). We foresee possible use of our densified plant cell biocomposites in panels for packaging or non–load-bearing automotive applications or space manufacturing.

We introduce a method to create natural biocomposite materials based on cultured plant cells. The method capitalizes on the plant cell's ability to synthesize intricate multilayered structures of cellulose, hemicellulose, phenolics, and pectin in their cell walls, which we preserve as nanostructured building blocks. In the future, the use of different cell cultures and/or genetically modified species (53), as well as the modulation of processing conditions to modify the cell arrangement at the microscale, may allow the fabrication of materials with significantly altered properties. Similar fabrication approaches can be envisioned for many other biological systems (e.g., algae and fungi) that can provide complex nanostructured elements as building blocks for advanced composite biomaterials.

Materials and Methods

Cell Cultures. Nicotiana tabacum Bright Yellow 2 (BY-2) cells were purchased from DSMZ. Cells were kept in Linsmaier & Skoog medium with vitamins (HIMEDIA-PT040) with 3% (wt/vol) sucrose at a pH of 5.8. The following supplements were added: 1 μM 2,4-dichlorophenoxyacetic acid (2,4-D), 1 μM a-naphthaleneacetic acid, and 1.46 mM KH_2PO_4. The cells were grown in 50 to
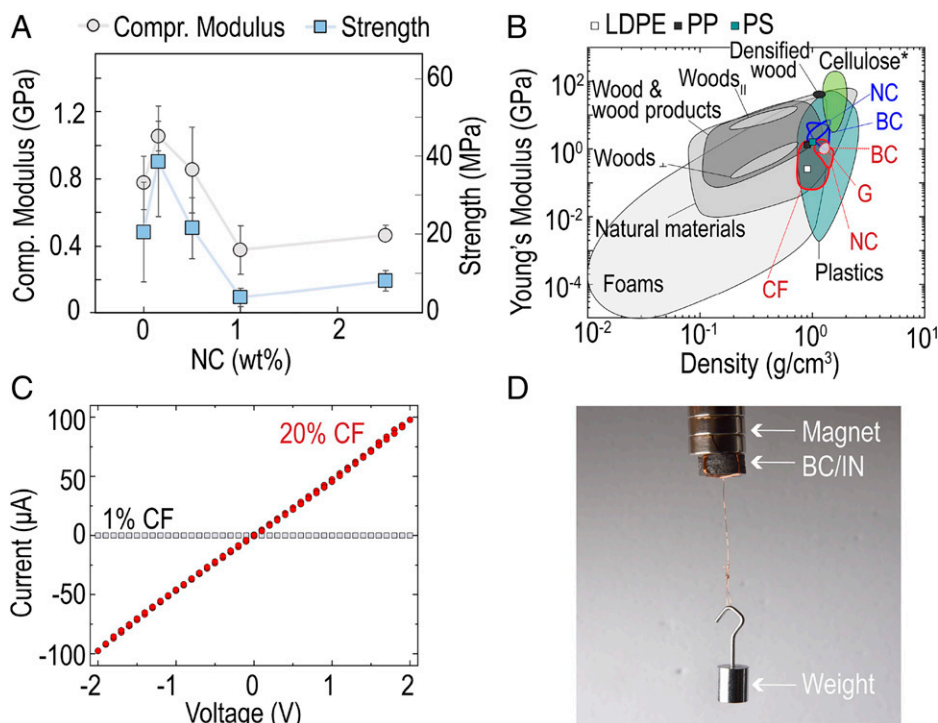

Fig. 4. (A) Compressive modulus and strength of biocomposites with NC platelets. (B) Young's modulus versus density for various materials and our biocomposites. Blue groups correspond to bending experiments, and red groups correspond to compression. The cellulose* area corresponds to pure cellulose fibers, papers, and nanocellulose-based products, including bacterial cellulose (37, 50, 51). Densified wood data are from ref. 20. (C) IV curves for biocomposites with 1 and 20 wt % CF. (D) Biocomposite with IN exhibiting magnetic properties.

300 mL aliquots in 100 mL to 1 L flasks on a rotary shaker (130 rpm) at room temperature and were subcultured biweekly at 1:10 to 1:60 dilutions.

Fabrication Method. Living cells were harvested and vacuum filtered in an Erlenmeyer flask, to remove water and growth media. The collected solid cell clusters were placed in porous aluminum custom designed molds (Metapor Aluminum) and subjected to a controlled compression. Pressure was gradually increased at a 0.1 ± 0.05 MPa/d rate to a maximum of 0.8 MPa, to compact the dehydrating cells until they reached a 2 ± 1 wt % solid residual mass. All samples were subsequently dried for 48 h at $60°$ C in a benchtop oven (Heratherm, Thermo Scientific). The residual water after the fabrication process was 7 ± 3 wt % as determined from thermogravimetric analysis measurements of the dried samples. Each sample density was calculated from the ratio of their mass (analytical balance XS205, Mettler Toledo) divided by their volume.

Materials. The natural wood materials tested were red oak (*Quercus rubra*), black walnut (*Juglans nigra*), yellow poplar (*Liriodendron tulipifera*), and sugar pine (*Pinus lambertiana*) and were kindly provided by California Institute of Technology (Caltech) resources. The engineered wood samples were hardwood plywood and medium-density untempered hardboard (MDF) provided by Caltech resources. The commercial plastics were LDPE (King Plastic Corp.), SIS-030E high-impact PS (Certene), and Densetec Copolymer PP (Polymer Industries).

Cell Staining. Cells were stained for cellulose in a 1% solution of alcian blue in 3% acetic acid (MilliporeSigma). The staining for pectin was performed using a 0.01% (vol/vol) ruthenium red solution in water, supplemented with 0.1% (vol/vol) ammonia (MilliporeSigma). We used safranin O in a 1% solution to stain phenolic compounds (MilliporeSigma).

Light Microscopy. A Zeiss Axio Scope A1 (Zeiss) was used for optical imaging of the untreated and stained cells. Two-photon analysis of the safranin-stained cells was performed in a Zeiss LSM 710 confocal laser scanning microscope (Zeiss). Image acquisition was implemented with a LC C-Apochromat $40\times/1.1$ W Korr M27 objective, at an excitation wavelength of 488 nm and emission wavelength 606 nm.

Electron Microscopy. SEM images were obtained using an FEI Nova 200 NanoLab Dualbeam Focused-Ion Beam/SEM (FEI), operating at 2 to 30 kV and 10 to 50 pA. For TEM, small sample pieces (1 to 2 mm^3) were fixed for 1 h with 2% OsO_4 in dH_2O. The pieces were rinsed $3\times$ with dH_2O, dehydrated into acetone over 48 h, then infiltrated with Epon-Araldite resin (Electron Microscopy Sciences) for 48 h. Then, 400 nm serial sections were cut with a UC6 μLtramicrotome (Leica Microsystems) using a diamond knife (Diatome US), placed on Formvar-coated copper-rhodium grids (Electron Microscopy Sciences) and stained with 3% aqueous uranyl acetate and lead citrate. Colloidal gold beads (10 nm) placed on both sides served as fiducial markers for subsequent image alignment. Grids were placed in a dual-axis tomography holder (Model 2040, E.A. Fischione Instruments, Inc.) and imaged with a TF-30ST electron microscope (ThermoFisher Scientific) at 300 keV. Images were recorded with US1000 camera (Gatan, Inc.) using the SerialEM software package (54), and the analysis was conducted using the IMOD software package (55).

FTIR Spectroscopy. FTIR spectra were collected with a ThermoNicolet iS10 spectrometer (Thermo Scientific) equipped with an attenuated total reflection crystal. We collected spectra of cells suspended in growth media, dried in the oven overnight at $60°$ C, and of the dry biocomposite. The spectra were collected across the range of 400 to 4,000 cm^{-1} with a resolution of 2 cm^{-1} and accumulated 64 scans for each spectrum.

Simulations. Reactive molecular dynamics simulations (ReaxFF) within the framework of Software for Chemistry and Materials (56) were used to simulate the interactions between hemicellulose, cellulose, pectin, and phenols within the cell walls of adjacent cells using the force field defined in ref. 57. The equilibrated system was composed of two compacted cell walls, following the compression step of the fabrication process. The final system was virtually tested in tension at strain rate of 1×10^8 s^{-1} pulling the two walls apart. The simulation setup is further documented in *SI Appendix*.

XRD. XRD patterns were collected using PANalytical X'Pert Pro (operating voltage at 40 kV, current at 40 mA, CuKα, $\lambda = 0.1541$ nm). An angular range of $2\theta = 10$ to $60°$ with a step size of $0.1°$ C and a scanning speed of $0.008°$ C s^{-1} was used for the measurements (Panalytical B.V.).

Chemical Analyses. Compositional analysis was carried out using the anthrone-sulfuric acid colorimetric method for cellulose, acidic hydrolysis for hemicellulose, the carbazole colorimetric method for pectin, and the klason method for phenolics.

Mechanical Properties Characterization. Three-point bending and tension tests were performed in an eXpert 8612 axial-torsion tester (Admet), an Instron 5500, and an Instron E3000. The biocomposite samples were tested with 250 N (for tensile tests) and 500 N load cells (for bending tests). For the flexural tests, a minimum of five samples of each material were tested at a constant strain rate of 0.004 ± 0.001 s^{-1} until failure. Samples of $\sim40 \times 5 \times 5$ mm (length $\times$ width $\times$ thickness) dimensions were tested in two perpendicular directions, as shown in *SI Appendix*, Fig. S6. Natural wood samples cut in $35 \times 7 \times 4$ mm strips and plastic samples cut at $75 \times 7 \times 4$ mm strips were tested at the same strain rate as the biocomposites. For the tensile tests a minimum of five samples were tested at a constant strain rate of 0.0025 ± 0.0001 s^{-1} until failure. We applied medium-density fiberboard end-tabs with dimensions $10 \times 10 \times 3$ mm in all $40 \times 5 \times 5$ mm specimens, using a thin layer of polyvinyl acetate adhesive (Gorilla Wood Glue). The natural wood tension samples, with dimensions $\sim100 \times 15 \times 5$ mm, and the plastic samples in a dog-bone configuration of $115 \times 1.5 \times 6$ mm (American Society for Testing and Materials [ASTM] D638, type IV) were tested at the same strain rate as the biocomposites. For the compression tests of the biocomposite samples, $\sim9 \times 9 \times 2$ mm (length $\times$ width $\times$ thickness) samples were tested under compression at a constant rate of 0.001 s^{-1} to a 10% target strain. The compressive modulus was calculated from the linear part of the unloading stress–strain curve, while the maximum stress value during compression, corresponding to the 10% strain, was referred to as compressive strength.

Biodegradation Tests. We characterized the biodegradability of the biocomposites and pine by incubating rectangular shaped pieces of 0.05 ± 0.01 g in agricultural soil (FoxFarm Ocean Forest Potting Soil). Each pot was stored in an outdoors location for 14 wk. The biocomposites and natural wood control samples were recovered every 2 wk to measure their residual mass. Following literature reported process (58), the samples were recovered, cleaned, and dried at room temperature and subsequently weighed.

Electrical Properties. Copper tape was used for the electrodes, connected to a Keithley 2636B source (Tektronix, Inc.). Voltage scans between -2 and 2 V, with a 0.1 V/s step were recorded. The slope of the obtained IV curves was converted to conductivity when multiplied with sample height and divided by cross-sectional area.

Water Uptake. Water uptake and thickness swelling tests were performed according to ASTM D1037 with appropriate modifications (18). Ten dry samples of $\sim4 \times 4$ mm were immersed in 5 mL of distilled water, and their relative mass and thickness increases were measured after 2 h.

Data Availability. All study data are included in the article and/or *SI Appendix*.

Author affiliations: ᵃDivision of Engineering and Applied Science, California Institute of Technology, Pasadena, CA 91125; ᵇDepartment of Materials Science and Engineering, University of Washington, Seattle, WA 98195; ᶜDepartment of Mechanical Engineering, University of Washington, Seattle, WA 98195; and ᵈDivision of Chemistry and Chemical Engineering, California Institute of Technology, Pasadena, CA 91125

1. A. K. Mohanty, M. Misra, G. Hinrichsen, Biofibres, biodegradable polymers and biocomposites: An overview. *Macromol. Mater. Eng.* **276–277**, 1–24 (2000).
2. A. K. Mohanty, S. Vivekanandhan, J. M. Pin, M. Misra, Composites from renewable and sustainable resources: Challenges and innovations. *Science* **362**, 536–542 (2018).
3. A. Mohanty, M. Misra, L. Drzal, *Natural Fibers, Biopolymers, and Biocomposites* (CRC Press, 2005).
4. O. Faruk, A. K. Bledzki, H. P. Fink, M. Sain, Biocomposites reinforced with natural fibers: 2000–2010. *Prog. Polym. Sci.* **37**, 1552–1596 (2012).
5. P. Q. Nguyen, N. D. Courchesne, A. Duraj-Thatte, P. Praveschotinunt, N. S. Joshi, Engineered living materials: Prospects and challenges for using biological systems to direct the assembly of smart materials. *Adv. Mater.* **30**, e1704847 (2018).
6. M. Schaffner, P. A. Rühs, F. Coulter, S. Kilcher, A. R. Studart, 3D printing of bacteria into functional complex materials. *Sci. Adv.* **3**, eaao6804 (2017).
7. C. Gilbert *et al.*, Living materials with programmable functionalities grown from engineered microbial co-cultures. *Nat. Mater.* **20**, 691–700 (2021).
8. P. A. Rühs, F. Storz, Y. A. L. Gómez, M. Haug, P. Fischer, 3d bacterial cellulose biofilms formed by foam templating. *npj Biofilms Microbiomes* **4**, 21 (2018).
9. R. A. Verlinden, D. J. Hill, M. A. Kenward, C. D. Williams, I. Radecka, Bacterial synthesis of biodegradable polyhydroxyalkanoates. *J. Appl. Microbiol.* **102**, 1437–1449 (2007).
10. S. Wang *et al.*, Super-strong, super-stiff macrofibers with aligned, long bacterial cellulose nanofibers. *Adv. Mater.* **29**, 1702498 (2017).
11. S. Wang *et al.*, Transparent, anisotropic biofilm with aligned bacterial cellulose nanofibers. *Adv. Funct. Mater.* **28**, 1707491 (2018).
12. M. Haneef *et al.*, Advanced materials from fungal mycelium: Fabrication and tuning of physical properties. *Sci. Rep.* **7**, 41292 (2017).
13. L. Valentini *et al.*, Fermentation based carbon nanotube multifunctional bionic composites. *Sci. Rep.* **6**, 27031 (2016).
14. N. M. Pugno, L. Valentini, Bionicomposites. *Nanoscale* **11**, 3102–3111 (2019).
15. M. Jones *et al.*, Thermal degradation and fire properties of fungal mycelium and mycelium-biomass composite materials. *Sci. Rep.* **8**, 17583 (2018).
16. E. Karana, D. Blauwhoff, E. J. Hultink, S. Camere, When the material grows: A case study on designing (with) mycelium-based materials. *Int. J. Des.* **12**, 119–136 (2018).
17. K. Cerimi, K. C. Akkaya, C. Pohl, B. Schmidt, P. Neubauer, Fungi as source for new bio-based materials: A patent review. *Fungal Biol. Biotechnol.* **6**, 17 (2019).
18. W. Sun, M. Tajvidi, C. G. Hunt, G. McIntyre, D. J. Gardner, Fully bio-based hybrid composites made of wood, fungal mycelium and cellulose nanofibrils. *Sci. Rep.* **9**, 3766 (2019).
19. L. J. Gibson, The hierarchical structure and mechanics of plant materials. *J. R. Soc. Interface* **9**, 2749–2766 (2012).
20. J. Song *et al.*, Processing bulk natural wood into a high-performance structural material. *Nature* **554**, 224–228 (2018).
21. L. A. Berglund, I. Burgert, Bioinspired wood nanotechnology for functional materials. *Adv. Mater.* **30**, e1704285 (2018).
22. F. Jiang *et al.*, Wood-based nanotechnologies toward sustainability. *Adv. Mater.* **30**, 1703453 (2018).
23. T. Li *et al.*, Anisotropic, lightweight, strong, and super thermally insulating nanowood with naturally aligned nanocellulose. *Sci. Adv.* **4**, eaar3724 (2018).
24. C. Chen *et al.*, Structure–property–function relationships of natural and engineered wood. *Nat. Rev. Mater.* **5**, 642–666 (2020).
25. T. Nagata, Y. Nemoto, S. Hasezawa, "Tobacco by-2 cell line as the "hela" cell in the cell biology of higher plants" in *International Review of Cytology*, K. W. Jeon, M. Friedlander, Eds. (Academic Press, 1992), **vol. 132**, pp. 1–30.
26. M. C. McCann, K. Roberts, Changes in cell wall architecture during cell elongation. *J. Exp. Bot.* **45**, 1683–1691 (1994).
27. M. C. McCann, J. Shi, K. Roberts, N. C. Carpita, Changes in pectin structure and localization during the growth of unadapted and NaCl-adapted tobacco cells. *Plant J.* **5**, 773–785 (1994).
28. Y. Yuan *et al.*, Microwave-assisted hydrothermal extraction of non-structural carbohydrates and hemicelluloses from tobacco biomass. *Carbohydr. Polym.* **223**, 115043 (2019).
29. Y. Zhang *et al.*, Molecular insights into the complex mechanics of plant epidermal cell walls. *Science* **372**, 706–711 (2021).
30. D. J. Cosgrove, Plant cell wall extensibility: Connecting plant cell growth with cell wall structure, mechanics, and the action of wall-modifying enzymes. *J. Exp. Bot.* **67**, 463–476 (2016).
31. M. C. McCann, N. J. Stacey, R. Wilson, K. Roberts, Orientation of macromolecules in the walls of elongating carrot cells. *J. Cell Biol.* **106**, 1347–1356 (1993).
32. Y. Hishikawa, E. Togawa, T. Kondo, Characterization of individual hydrogen bonds in crystalline regenerated cellulose using resolved polarized FTIR spectra. *ACS Omega* **2**, 1469–1476 (2017).
33. S. Cichosz, A. Masek, IR study on cellulose with the varied moisture contents: Insight into the supramolecular structure. *Materials (Basel)* **13**, 4573 (2020).
34. A. Peaucelle, R. Wightman, H. Höfte, The control of growth symmetry breaking in the Arabidopsis hypocotyl. *Curr. Biol.* **25**, 1746–1752 (2015).
35. H. Zhu *et al.*, Anomalous scaling law of strength and toughness of cellulose nanopaper. *Proc. Natl. Acad. Sci. U.S.A.* **112**, 8971–8976 (2015).
36. Q. Meng, T. J. Wang, Mechanics of strong and tough cellulose nanopaper. *Appl. Mech. Rev.* **71**, 040801 (2019).
37. R. J. Moon, A. Martini, J. Nairn, J. Simonsen, J. Youngblood, Cellulose nanomaterials review: Structure, properties and nanocomposites. *Chem. Soc. Rev.* **40**, 3941–3994 (2011).
38. A. Mittal, R. Katahira, M. E. Himmel, D. K. Johnson, Effects of alkaline or liquid-ammonia treatment on crystalline cellulose: Changes in crystalline structure and effects on enzymatic digestibility. *Biotechnol. Biofuels* **4**, 41 (2011).
39. Y. Liao *et al.*, The role of pretreatment in the catalytic valorization of cellulose. *Mol. Catal.* **487**, 110883 (2020).
40. L. Valentini, S. Bittolo Bon, S. Signetti, N. M. Pugno, Graphene-based bionic composites with multifunctional and repairing properties. *ACS Appl. Mater. Interfaces* **8**, 7607–7612 (2016).
41. L. Valentini, S. Bittolo Bon, N. M. Pugno, Graphene and carbon nanotube auxetic rubber bionic composites with negative variation of the electrical resistance and comparison with their nonbionic counterparts. *Adv. Funct. Mater.* **27**, 1606526 (2017).
42. R. Di Giacomo *et al.*, Candida albicans/MWCNTs: A stable conductive bio-nanocomposite and its temperature-sensing properties. *IEEE Trans. NanoTechnol.* **12**, 111–114 (2013).
43. R. Di Giacomo, C. Daraio, B. Maresca, Plant nanobionic materials with a giant temperature response mediated by pectin-Ca2+. *Proc. Natl. Acad. Sci. U.S.A.* **112**, 4541–4545 (2015).
44. R. Di Giacomo *et al.*, Bio-nano-composite materials constructed with single cells and carbon nanotubes: Mechanical, electrical, and optical properties. *IEEE Trans. NanoTechnol.* **12**, 1026–1030 (2013).
45. A. Manjula-Basavanna, A. Duraj-Thatte, N. S. Joshi, Robust self-regeneratable stiff living materials fabricated from microbial cells. *Adv. Funct. Mater.* **31**, 2010784 (2021).
46. K. G. Satyanarayana, G. G. Arizaga, F. Wypych, Biodegradable composites based on lignocellulosic fibers–An overview. *Prog. Polym. Sci.* **34**, 982–1021 (2009).
47. K. Iiyama, T. Lam, B. A. Stone, Covalent cross-links in the cell wall. *Plant Physiol.* **104**, 315–320 (1994).
48. F. Natalio *et al.*, Biological fabrication of cellulose fibers with tailored properties. *Science* **357**, 1118–1122 (2017).
49. F. Natalio, Biological fabrication: Future perspectives on biological fabrication and material farming (small methods 1/2019). *Small Methods* **3**, 1800055 (2019).
50. A. J. Benítez, A. Walther, Cellulose nanofibril nanopapers and bioinspired nanocomposites: A review to understand the mechanical property space. *J. Mater. Chem. A Mater. Energy Sustain.* **5**, 16003–16024 (2017).
51. Y. C. Hsieh, H. Yano, M. Nogi, S. Eichhorn, An estimation of the young's modulus of bacterial cellulose filaments. *Cellulose* **15**, 507–513 (2008).
52. E. Roumeli *et al.*, Factors controlling the enhanced mechanical and thermal properties of nanodiamond-reinforced cross-linked high density polyethylene. *J. Phys. Chem. B* **118**, 11341–11352 (2014).
53. E. Roumeli *et al.*, Structure and biomechanics during xylem vessel transdifferentiation in Arabidopsis thaliana. *Plants* **9**, 1715 (2020).
54. D. N. Mastronarde, Automated electron microscope tomography using robust prediction of specimen movements. *J. Struct. Biol.* **152**, 36–51 (2005).
55. D. N. Mastronarde, Correction for non-perpendicularity of beam and tilt axis in tomographic reconstructions with the IMOD package. *J. Microsc.* **230**, 212–217 (2008).
56. A. C. T. van Duin, S. Dasgupta, F. Lorant, W. A. Goddard, Reaxff: A reactive force field for hydrocarbons. *J. Phys. Chem. A* **105**, 9396–9409 (2001).
57. A. Vashisth, C. Ashraf, W. Zhang, C. E. Bakis, A. C. T. van Duin, Accelerated ReaxFF simulations for describing the reactive cross-linking of polymers. *J. Phys. Chem. A* **122**, 6633–6642 (2018).
58. H. Wang, D. Wei, A. Zheng, H. Xiao, Soil burial biodegradation of antimicrobial biodegradable PBAT films. *Polym. Degrad. Stabil.* **116**, 14–22 (2015).